Room Temperature Structural and Electrical Studies on Jahn-Teller Distortions Signal Induced by Cr and Co Doping in $Pr_{0.75}Na_{0.2}Ag_{0.05}Mn_{1-x}M_xO_3$ Perovskite Manganites

Wen Lin Teo
Ceramic and Amorphous Group, Faculty of Applied Sciences and Technology, Universiti Tun Hussein Onn Malaysia, Pagoh, Malaysia
gw240024@student.uthm.edu.my

Suhadir Shamsuddin
Ceramic and Amorphous Group, Faculty of Applied Sciences and Technology, Universiti Tun Hussein Onn Malaysia, Pagoh, Malaysia
suhadir@uthm.edu.my (corresponding author)

Saifful Kamaluddin Muzakir
Faculty of Industrial Sciences and Technology, Universiti Malaysia Pahang Al-Sultan Abdullah, Gambang, Pahang, Malaysia
saifful@umpsa.edu.my

Mirza Basyir Rodhuan
Faculty of Industrial Sciences and Technology, Universiti Malaysia Pahang Al-Sultan Abdullah, Gambang, Pahang, Malaysia
pmz24002@adab.umpsa.edu.my

Received: 8 March 2025 | Revised: 10 May 2025 and 1 June 2025 | Accepted: 6 June 2025

 DOI: https://doi.org/10.48084/etasr.10808

ABSTRACT

In this study, $Pr_{0.75}Na_{0.2}Ag_{0.05}Mn_{1-x}M_xO_3$ (M=Cr, Co) (x = 0, 0.02, and 0.05) samples were synthesized via the standard solid-state method with magnetic ion (Cr, Co) doping. The study aimed to investigate the crystalline phase, surface morphology, and resistivity, addressing the lack of experimental data related to Jahn-Teller (JT) distortion in such systems. Structural, morphological, and electrical characterizations were performed using X-ray Diffraction (XRD), Scanning Electron Microscopy with Energy-Dispersive X-ray (SEM-EDX) spectroscopy, Fourier Transform Infrared Spectroscopy (FTIR), and four-point probe measurements. All samples crystallized in an orthorhombic structure with a Pnma space group, with lattice parameters decreasing as Cr and Co doping concentrations increased. SEM observations revealed that grain boundaries became more compact, accompanied by a reduction in grain size. FTIR spectra confirmed Mn–O stretching vibrations at 703 cm^{-1}, 711 cm^{-1}, 714 cm^{-1}, 726 cm^{-1}, and 727 cm^{-1} for Pr-1, Pr-2, Pr-3, Pr-4, and Pr-5, respectively. Resistivity measurements showed a decrease with doping, attributed to the reduced interaction distance between atoms. Overall, minor Cr and Co substitutions appear to weaken the JT distortion by replacing Mn^{3+} ions, as supported by the experimental findings.

Keywords-doping induced; Jahn-Teller distortion; perovskite manganite

I. INTRODUCTION

The discovery of the Colossal Magnetoresistance (CMR) effect in perovskite manganites with the general formula ABO_3 (where A is the trivalent rare-earth ion or divalent alkaline earth ion) has garnered significant attention due to their remarkable physical properties and potential applications. These materials have been investigated for use in medical, biological, and technological applications, including stable electrodes [1], magnetic refrigeration systems [2], and electrode materials for supercapacitors [3]. Among these, magnetic refrigeration systems are particularly notable due to their enhanced energy efficiency and reduced environmental impact [4].

Research on rare-earth manganites has attributed the CMR effect primarily to the Double-Exchange (DE) mechanism [5], the Jahn-Teller (JT) effect [6], and Charge Ordering (CO) [7]. Further studies have demonstrated that monovalent doping at the A-site of perovskite manganites results in a mixed Mn^{3+}/Mn^{4+} state, promoting possible interactions such as Mn^{3+}-O^{2-}-Mn^{3+}, Mn^{4+}-O^{2-}-Mn^{4+}, and Mn^{3+}-O^{2-}-Mn^{4+}. The latter occurs through electron hopping from Mn^{3+} ion to Mn^{4+} ion via O^{2-} ion, combined with coupling between s-d and s-s electrons, leading to a Ferromagnetic (FM) interaction [8, 9].

Although perovskite manganites typically exhibit Antiferromagnetic (AFM) ordering, their specific properties can be tailored through doping at either the A-site or B-site or varying sintering temperatures. Literature indicates that A-site doping has been extensively studied for its impact on magnetic and transport properties. For instance, polycrystalline $Pr_{0.75}Na_{0.2-y}Ag_yMnO_3$ manganites display notable structural, morphological, electrical, and magnetic properties [10]. These samples crystallize in an orthorhombic structure with a Pnma space group, where increasing Ag doping leads to reduced lattice parameters and increased porosity. Specifically, the y=0.05 sample exhibits a Ferromagnetic-Metallic (FMM) phase due to the DE mechanism, which weakens the CO state. In contrast, other compositions show insulating behavior with Paramagnetic-to-Antiferromagnetic (PM-AFM) transitions, with Néel temperatures T_N~125 K and T_N~126 K, respectively [11]. Similarly, in $La_{1-y}Sr_yMn_{0.5}Co_{0.5}O_3$ ($0<y<0.5$), resistivity decreases with increasing Sr-doping, likely due to high-spin stabilized Co^{3+} ions enhancing FM interactions [3]. However, limited information is available on the JT effects of B-site doping in monovalent-doped manganites

Reports indicate that direct B-site substitution with small amounts of transition-metal ions significantly affects physical properties by modifying structural parameters such as bond angles, bond lengths, lattice distortions, and the tolerance factor [12]. This can induce a Metal-Insulator (MI) transition in CO undoped insulators and produce a large CMR effect, especially with Cr^{3+} ions. For example, in $Nd_{0.7}Sr_{0.3}Mn_{1-x}Cr_xO_3$ and $La_{0.7}Ca_{0.3}Mn_{1-x}Cr_xO_3$, the MI transition shifts to higher temperatures due to enhanced DE interactions between Mn^{3+}-O^{2-}-Mn^{4+} [13]. Likewise, $Nd_{0.5}Ca_{0.5}Mn_{1-x}Cr_xO_3$ shows a higher MI transition temperature associated with the CO state [14]. These changes correspond to shifts in the Paramagnetic–Ferromagnetic (PM–FM) transition. Furthermore, B-site doping can alter the microstructure through JT distortions caused by reduced oxygen bond lengths following Mn-ion substitution.

Despite these findings, studies on elemental substitution at the Mn-site remain limited. To the best of our knowledge, the effects of Cr and Co doping at the Mn-site of $Pr_{0.75}Na_{0.2}Ag_{0.05}Mn_{1-x}M_xO_3$ (M=Cr, Co) on structural, morphological, and room-temperature electrical resistivity properties have not been comprehensively reported. This work investigates these effects, with particular attention to the role of the isoelectronic states of Mn^{3+}, Cr^{3+}, and Co^{3+} in influencing JT distortion. Additionally, this study reports density and porosity measurements for the synthesized samples.

II. MATERIALS

Polycrystalline samples of $Pr_{0.75}Na_{0.2}Ag_{0.05}Mn_{1-x}M_xO_3$ (M=Cr, Co) (x = 0, 0.02, and 0.05) were synthesized using the standard solid-state reaction method without any impurity phase [15], which involved processes such as mixing and grinding stoichiometric amounts of high purity (≥99.99%) Pr_6O_{11}, Na_2CO_3, Ag_2O, MnO_2, Co_3O_4, and Cr_2O_3 powders. The chemical powders were thoroughly mixed and ground with an agate mortar and pestle. The mixture was then calcined in air at 1000 °C for approximately 24 hours intermittent regrinding to ensure homogeneity. The calcined powders were pressed into pellets under 5 tons of pressure for 15 min and sintered in air at 1200 °C for 24 hours to obtain the following compositions:

- $Pr_{0.75}Na_{0.2}Ag_{0.05}MnO_3$ (Pr-1).
- $Pr_{0.75}Na_{0.2}Ag_{0.05}Mn_{0.98}Cr_{0.02}O_3$ (Pr-2).
- $Pr_{0.75}Na_{0.2}Ag_{0.05}Mn_{0.95}Cr_{0.05}O_3$ (Pr-3).
- $Pr_{0.75}Na_{0.2}Ag_{0.05}Mn_{0.98}Co_{0.02}O_3$ (Pr-4).
- $Pr_{0.75}Na_{0.2}Ag_{0.05}Mn_{0.95}Co_{0.05}O_3$ (Pr-5).

The crystal structure of the samples was examined using Powder X-ray Diffraction (XRD) with a Bruker D2 Phaser instrument, employing CuKα radiation (λ = 1.54 Å) at room temperature. The surface morphology and elemental composition were characterized using a COXEM EM-30AX PLUS Scanning Electron Microscope (SEM) equipped with Energy Dispersive X-ray Spectroscopy (EDX). Fourier Transform Infrared (FTIR) transmittance measurements were performed using an Agilent Cary 630 FTIR spectrometer within the wavenumber range of 600-1200 cm^{-1} to investigate the metal-oxide bonding. The electrical resistivity of the synthesized samples was measured at room temperature using the four-point probe method (SR–4 4PP). The bulk density ρ_{bulk} of each sample was determined according to Archimedes' principle, using propanol as the buoyant medium, following (1):

$$\rho_{bulk} = \frac{\omega_{\text{air}}}{\omega_{air}\omega_{propanol}}\rho_{propanol} \quad (1)$$

where ω_{air} is the weight of the sample in air, $\omega_{propanol}$ is the weight of the sample in propanol, and $\rho_{propanol}$ is the density of propanol. The porosity (%) of the samples was calculated using (2):

$$\text{Porosity (\%)} = 1 - \frac{\rho_{bulk}}{\rho_{particle}} 100\% \quad (2)$$

where $\rho_{particle}$ is the particle density obtained from (3):

$$\rho_{particle} = \frac{n'(\Sigma A_C + \Sigma A_A)}{V_C N_A} \quad (3)$$

where n' is the number of formula units, ΣA_C is the sum of the atomic weights of all cations, ΣA_A is the sum of the atomic weights of all anions, V_C is the volume of the unit cell, and N_A is Avogadro's number.

III. RESULTS AND DISCUSSION

Figure 1(a) presents the powder XRD patterns of Pr-1, Pr-2, Pr-3, Pr-4, and Pr-5, confirming that all samples crystallize in a single-phase orthorhombic structure (space group Pnma) without detectable impurities, consistent with earlier reports [16, 17]. Figure 1(b) shows the (220) diffraction peak shifting toward higher angles, indicating a reduction in unit cell volume. Table I lists the lattice parameters, unit cell volume (V), bulk density (D), porosity (ϕ), resistivity (ρ), and average grain size for all samples. Lattice parameters were determined from Bragg's law and the orthorhombic interplanar spacing equation:

$$n\lambda = 2d\sin\theta \quad (4)$$

$$\frac{1}{d^2} = \frac{h^2}{a^2} + \frac{k^2}{b^2} + \frac{l^2}{c^2} \quad (5)$$

where n is the diffraction order, λ is the wavelength of the X-rays, d is the interplanar spacing, θ is the diffraction angle, h, k, and l are Miller indices, and a, b, and c are the orthorhombic lattice parameters.

Both a, b, and c decrease progressively with Cr or Co doping, accompanied by a reduction in V from 232.3 Å^3 (Pr-1) to 231.7 Å^3 (Pr-3) for Cr doping and to 231.1 Å^3 (Pr-5) for Co doping. This reduction is linked to the ionic radii of the host and dopant atoms. The replacement of the larger ionic size of Mn^{3+} ($e_g^1\ t_{2g}^3$; 0.645 Å) with the smaller ionic radius of Cr^{3+} ($e_g^0\ t_{2g}^3$; 0.615 Å) and Co^{3+} ($e_g^0\ t_{2g}^6$; 0.545 Å) ions leads to the lattice distortion and causes a reduction in lattice parameters, and hence volume [18]. To maintain charge neutrality, Mn^{3+} ions are partially oxidized to Mn^{4+} (t_{2g}^3; 0.530 Å) [19]. The increase in Mn^{4+} fraction disrupts Mn^{3+}-O^{2-}-Mn^{4+} superexchange, alters density and porosity, and reduces room-temperature resistivity [20, 21]. Smaller grain size and lower porosity enhance Mn^{4+}-mediated double exchange, facilitating electron hopping through Mn-O-Mn pathways and suppressing JT distortion [8].

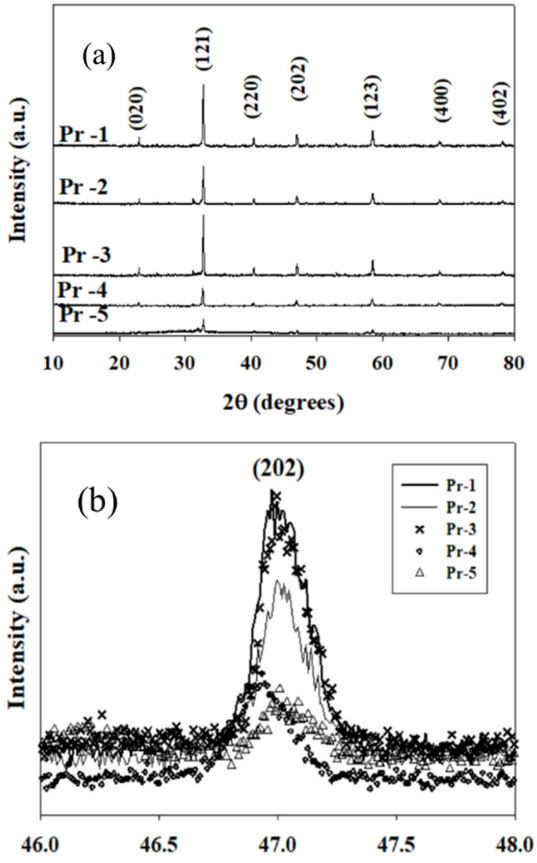

Fig. 1. (a) Powder XRD pattern for $Pr_{0.75}Na_{0.2}Ag_{0.05}Mn_{1-x}(Cr, Co)_xO_3$ samples, (b) XRD diffraction pattern at 47.0° for undoped sample (Pr-1) and doped samples (Pr-2, Pr-3, Pr-4, Pr-5)

TABLE I. THE PROPERTIES $PR_{0.75}NA_{0.2}AG_{0.05}MN_{1-X}(CR, CO)_XO_3$

Samples	Lattice Parameter (±0.001)			V (Å^3)	D (g/cm^3)	ϕ (%)	ρ (Ω)	Grain Size (μm)
	a (Å)	*b* (Å)	*c* (Å)	(±0.1)	(±0.001)	(±0.01)	(±0.1)	(±0.001)
Pr-1	5.474	7.753	5.474	232.3	5.889	13.73	113.1	6.643
Pr-2	5.473	7.749	5.467	231.9	5.332	16.34	108.3	5.814
Pr-3	5.472	7.748	5.466	231.7	5.301	17.45	107.9	5.368
Pr-4	5.470	7.747	5.466	231.6	5.600	19.08	106.7	5.596
Pr-5	5.468	7.738	5.462	231.1	5.680	18.16	97.09	5.315

Figure 2(a) shows SEM micrographs at 2000× magnification alongside a 3D structural model of the perovskite lattice from XRD data using VESTA software [22]. The average grain size of samples was estimated using the ImageJ software [23], and values are shown in Table I. Figure 2(b) shows the normal grain size distribution graph of Pr-1 based on SEM and ImageJ data.

Cr^{3+} and Co^{3+} substitution leads to smaller, more compact grains due to reduced ionic radius compared to Mn^{3+}. For Cr-doped samples, the average grain size decreases from 6.643 μm (Pr-1) to 5.368 μm (Pr-3). For Co doping, the grain size drops from 5.596 μm (Pr-4) to 5.315 μm (Pr-5). Pr-1 exhibits irregular grains with visible porosity, while doped samples show denser boundaries, consistent with reduced JT distortion

[24]. Figure 3, showing the EDX spectra for all the samples, confirms the presence of all expected elements (Pr, Na, Ag, Cr, Co, Mn, O) without impurities, verifying successful doping, and especially the presence of Cr and Co elements in the samples, indicating the incorporation of dopants in the manganite compounds.

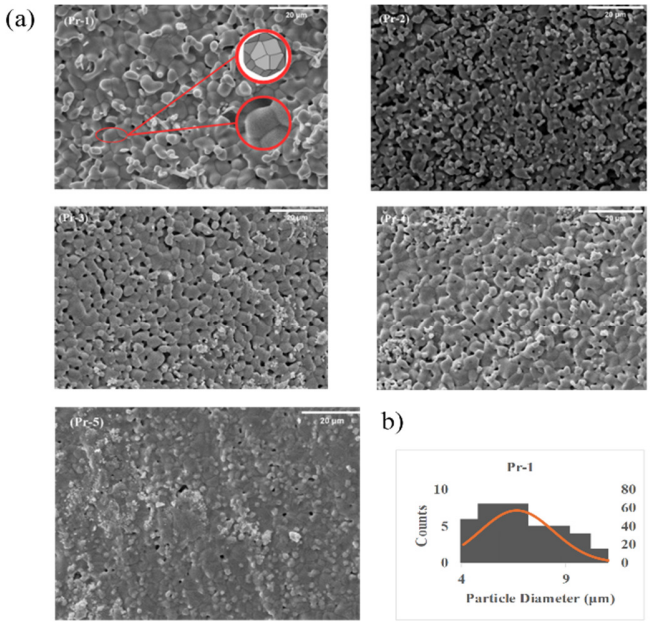

Fig. 2. (a) SEM images of magnification 2000× and 20µm for Pr-1, Pr-2, Pr-3, Pr-4, and Pr-5 samples, (b) Average grain size distribution of sample Pr-1.

The FTIR analysis provided insights into the elemental composition, chemical bonding, stretching modes, and vibrational frequencies of the prepared samples. In perovskite manganite structures, the fundamental IR absorption bands are typically associated with MnO_6 octahedral, corresponding to Mn-O bond vibrations in the range of 400-750 cm^{-1} [25]. As shown in Figure 4, the FTIR spectrum of the Pr-1 sample exhibits a broad peak at 703 cm^{-1}, indicating the presence of strong metal–oxygen bonds. These bands arise from stretching or bending vibration modes, as reported in previous studies [26–28]. Upon doping Cr and Co into the Mn site, the absorption peaks shift toward higher wavenumbers. This shift suggests a weakening of the Mn-O stretching mode, attributed to the incorporation of smaller ions at the Mn site, which induces lattice distortion and reduces the unit cell volume. Consequently, the force constant of the vibrational bands increases, producing a blue shift in the IR spectra. The observed ionic radii decrease in the order Mn^{3+} (0.645 Å, Pr-1) > Cr^{3+} (0.615 Å, Pr-2, Pr-3) > Co^{3+} (0.545 Å, Pr-4, Pr-5), with corresponding peak positions at 703 cm^{-1}, 711 cm^{-1}, 714 cm^{-1}, 726 cm^{-1}, and 727 cm^{-1}, respectively. These results indicate that Cr and Co doping leads to a reduction in Mn-O bond length, consistent with JT distortion effects, as supported by the XRD and SEM findings.

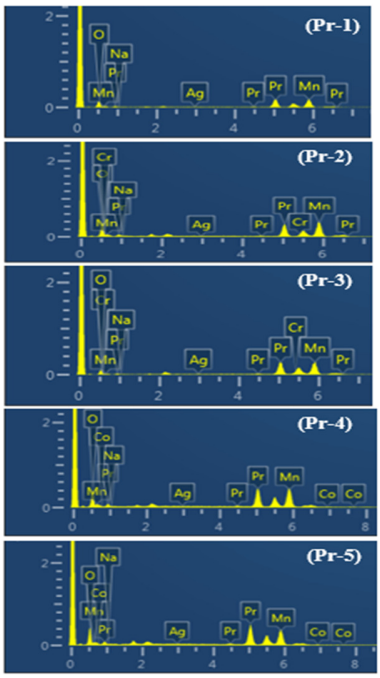

Fig. 3. The EDX spectra of Pr-1, Pr-2, Pr-3, Pr-4, and Pr-5 manganite samples.

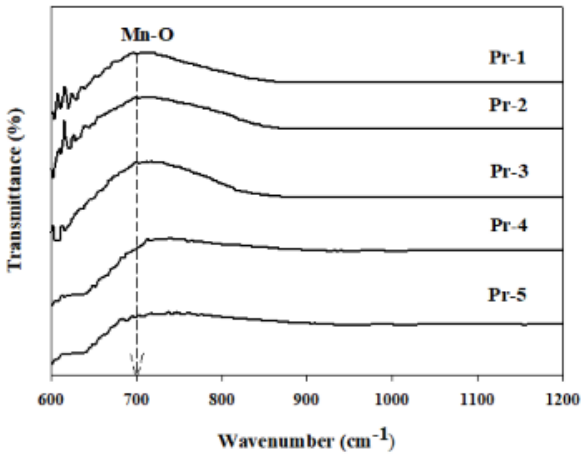

Fig. 4. The FTIR spectrum of Pr-1, Pr-2, Pr-3, Pr-4, and Pr-5 samples.

IV. CONCLUSION

In conclusion, a detailed investigation of the structural properties of $Pr_{0.75}Na_{0.2}Ag_{0.05}Mn_{1-x}(Cr, Co)_xO_3$ was conducted to evaluate the effects of Cr and Co doping. X-ray Diffraction (XRD) results confirmed that all samples crystallized in an orthorhombic structure with the Pnma space group, with no alteration to the overall structural arrangement, consistent with previous studies. Substitution of smaller Cr^{3+} or Co^{3+} ions at the Mn-site led to oxidation of Mn^{3+} to Mn^{4+} for charge neutrality, resulting in lattice distortion. Among the dopants, Co^{3+} (0.545 Å) produced the smallest grain volume (x = 0.05) due to its shorter bond length compared to Cr^{3+} (0.615 Å).

Surface morphology analysis revealed that doping with smaller ions increased grain boundary compaction and reduced

grain size, with Co-doping producing a more compact and flat surface structure than Cr-doping. Fourier Transform Infrared Spectroscopy (FTIR) spectra confirmed the perovskite manganite structure and exhibited a blue-shift in the Mn-O vibrational bands, indicating lattice compression and a reduction in Mn-O bond length. These findings support the conclusion that Cr and Co doping weakens the Jahn-Teller (JT) effect by decreasing the electron hopping distance within the lattice.

Room-temperature resistivity measurements showed a decrease in resistivity upon doping, attributed to reduced porosity and an increased Mn^{4+}/Mn^{3+} ratio. This enhancement in the Double-Exchange (DE) mechanism facilitates electron hopping between Mn-O bonds, further weakening the JT distortion. Consequently, minor doping at the Mn-site not only improves charge mobility and electrical conductivity but also promotes a transition from insulating to more metallic behavior at room temperature. These effects make the doped compounds promising candidates for spintronic and other energy-related applications.

ACKNOWLEDGMENT

This research was supported by the Geran Penyelidikan Pascasiswazah (GPPS), vot Q793, Faculty of Applied Sciences and Technology (FAST), Universiti Tun Hussein Onn Malaysia (UTHM), under grant E15203, and by the UTHM Publisher's Office through the Publication Fund E15216.

REFERENCES

[1] T. Chahar, A. Somvanshi, and A. Khan, "Structural and surface morphological investigation of Ni-doped $NdMnO_3$ perovskite nanomaterial," *Materials Today: Proceedings*, Mar. 2023, https://doi.org/10.1016/j.matpr.2023.03.118.

[2] M. R. Khatun *et al.*, "A combined experimental and computational approach on $La_{0.6}Sr_{0.4}MnO_3$ perovskite," *Materials Chemistry and Physics*, vol. 295, Feb. 2023, Art. no. 127163, https://doi.org/10.1016/j.matchemphys.2022.127163.

[3] M. L. Syauqi, A. R. Sanjaya, M. J. Madiabu, M. Khalil, and J. Gunlazuardi, "TiO_2 Crystallization at Room Temperature and Preparation of Transparent Carbon Counter Electrode for Low-Cost Dye-Sensitized Solar Cells," *Makara Journal of Science*, vol. 27, no. 2, Jun. 2023, https://doi.org/10.7454/mss.v27i2.1476.

[4] P. R. Nadig, O. Toulemonde, P. Alagarsamy, M. S. Murari, and M. D. Daivajna, "Multifaceted Roles of Ag^+ Ions within and outside La–Ca–MnO_3 Perovskite Manganites: Unveiling the Room Temperature Magnetocaloric Effect," *The Journal of Physical Chemistry C*, vol. 128, no. 30, pp. 12686–12703, Aug. 2024, https://doi.org/10.1021/acs.jpcc.4c03215.

[5] U. A. Palikundwar, K. R. Nagde, C. M. Dudhe, and G. C. Wakde, "Effect of Sr doping on structural, magnetic and transport properties of La_1-y$SryMn_{0.5}Co_{0.5}O_3$±δ," *Physica B: Condensed Matter*, vol. 657, May 2023, Art. no. 414823, https://doi.org/10.1016/j.physb.2023.414823.

[6] A. Kandemir, G. Akça, S. Kılıç Çetin, A. O. Ayaş, M. Akyol, and A. Ekicibil, "Effects of Ca substitution on magnetic and magnetocaloric properties in $PrBa_1$-x$CaxMn_2O_6$ system," *Journal of Solid State Chemistry*, vol. 324, Aug. 2023, Art. no. 124086, https://doi.org/10.1016/j.jssc.2023.124086.

[7] P. Amalthi, J. J. Vijaya, R. Thinesh Kumar, L. John Kennedy, M. Bououdina, and B. Saravanakumar, "Microwave-aided fabrication of calcium-substituted $DyMnO_3$ nanocomposites as prospective battery-type electrode material for supercapacitors," *Materials Science and Engineering: B*, vol. 298, Dec. 2023, Art. no. 116845, https://doi.org/10.1016/j.mseb.2023.116845.

[8] W. Hizi, H. Rahmouni, K. Khirouni, and E. Dhahri, "Investigation of charge-carriers dynamics and sub/super-linear response for La0.8Na0.2-x□xMnO_3 (x = 0 and 0.1) perovskite ceramics," *Physica B: Condensed Matter*, vol. 673, Jan. 2024, Art. no. 415423, https://doi.org/10.1016/j.physb.2023.415423.

[9] A. Rahman *et al.*, "Comprehensive approach on La1-$PbMnO_3$ ($0.2 \leq x \leq 0.5$) perovskites synthesized by solid state reaction technique," *Journal of Alloys and Compounds*, vol. 1010, Jan. 2025, Art. no. 177373, https://doi.org/10.1016/j.jallcom.2024.177373.

[10] N. Khairulzaman, N. Ibrahim, and S. Shamsuddin, "Impact of Ag-Doped on the Ferromagnetic-Metallic Transition in $Pr_{0.75}Na_{0.25}MnO_3$ Manganites," *International Journal of Engineering & Technology*, vol. 7, no. 4.30, pp. 68–71, Nov. 2018, https://doi.org/10.14419/ijet.v7i4.30.22011.

[11] S. Shamsuddin, N. Ibrahim, M. Z. H. Mayzan, F. Esa, and S. A. Razali, "Analysis of Electrical Transport Properties in $Nd_{0.75}Na_{0.25-x}K_xMnO_3$ Manganites," in *Proceedings of the 7th International Conference on the Applications of Science and Mathematics 2021*, Singapore, 2022, vol. 273, pp. 139–145, https://doi.org/10.1007/978-981-16-8903-1_14.

[12] D. A. Rueda *et al.*, "Evidence of multifunctional properties of ferromanganite $La_{0.5}Ca_{0.5}Mn_{0.5}Fe_{0.5}O_3$," *Journal of Molecular Structure*, vol. 1314, Oct. 2024, Art. no. 138821, https://doi.org/10.1016/j.molstruc.2024.138821.

[13] N. Kumar, A. Rao, V. P. S. Awana, A. B. Garg, R. Mittal, and R. Mukhopadhyay, "Mixed-exchange: Cr & Fe Doped $La_{0.7}Ca_{0.3}MnO_3$," presented at the Solid State Physics, *Proceedings Of The 55th Dae Solid State Physics Symposium 2010*, Manipal, (India), 2011, pp. 989–990, https://doi.org/10.1063/1.3606192.

[14] N. N. A. Mannan, S. A. Razali, S. Shamsuddin, and M. Z. Noh, "Crystalline Phase, Surface Morphology and Electrical Properties of Monovalent-doped $Nd_{0.75}Na_{0.25}Mn_{1-y}Co_yO_3$ Manganites," *Journal of Science and Technology*, vol. 9, no. 3, pp. 65–69, Nov. 2017.

[15] A. K. Agrawal *et al.*, "Structural, optical absorption and electrical characteristics of sol-gel synthesized chromium-doped bismuth ferrites," *Physica B: Condensed Matter*, vol. 696, Jan. 2025, Art. no. 416639, https://doi.org/10.1016/j.physb.2024.416639.

[16] A. Haoui, M. Elchikh, S. Hiadsi, and A. Hireche Baghdad, "DFT analysis of mechanical, thermal, half-metallic, and thermoelectric properties of perovskites $PrMnO_3$ and $NdMnO_3$ ortho-manganite," *Physica B: Condensed Matter*, vol. 684, Jul. 2024, Art. no. 416001, https://doi.org/10.1016/j.physb.2024.416001.

[17] P. R. Nadig, M. M. S., and M. D. Daivajna, "Influence of heat sintering on the physical properties of bulk $La_{0.67}Ca_{0.33}MnO_3$ perovskite manganite: role of oxygen in tuning the magnetocaloric response," *Physical Chemistry Chemical Physics*, vol. 26, no. 6, pp. 5237–5252, 2024, https://doi.org/10.1039/D3CP04185A.

[18] A. N. Ganie, I. Irshad, M. U. D. Rather, and B. Want, "Delving into the structural, electric, and electrochemical properties of Yb^{3+} and Cr^{3+} co-doped $BiFeO_3$ nanostructures for supercapacitor applications," *Journal of Alloys and Compounds*, vol. 1018, Mar. 2025, Art. no. 179229, https://doi.org/10.1016/j.jallcom.2025.179229.

[19] T. Kocak, L. Wu, J. Wang, U. Savaci, S. Turan, and X. Zhang, "The effect of vanadium doping on the cycling performance of $LiNi_{0.5}Mn_{1.5}O_4$ spinel cathode for high voltage lithium-ion batteries," *Journal of Electroanalytical Chemistry*, vol. 881, Jan. 2021, Art. no. 114926, https://doi.org/10.1016/j.jelechem.2020.114926.

[20] W. Zhang, Z. Xie, Z. Zou, X. Jiang, C. Xu, and M. Feng, "Eu/Ni doping on the structure, magnetocaloric effect and critical behaviour of $La_{0.65}Sr_{0.35}MnO_3$ ceramics," *Ceramics International*, vol. 50, no. 3, pp. 4921–4935, Feb. 2024, https://doi.org/10.1016/j.ceramint.2023.11.235.

[21] M. M. Gomaa, "Effect of grain shape elongation in direction and perpendicular to current stream (conductive or insulator) on the electrical characteristics of mixtures," *Scientific Reports*, vol. 15, no. 1, Jan. 2025, Art. no. 1596, https://doi.org/10.1038/s41598-024-83223-8.

[22] K. Momma and F. Izumi, "*VESTA 3* for three-dimensional visualization of crystal, volumetric and morphology data," *Journal of Applied Crystallography*, vol. 44, no. 6, pp. 1272–1276, Dec. 2011, https://doi.org/10.1107/S0021889811038970.

[23] C. A. Schneider, W. S. Rasband, and K. W. Eliceiri, "NIH Image to ImageJ: 25 years of image analysis," *Nature Methods*, vol. 9, no. 7, pp. 671–675, Jul. 2012, https://doi.org/10.1038/nmeth.2089.

[24] K. Ramya, S. Bharadwaj, S. Pola, G. S. Okram, and Y. Kalyanalakshmi, "Effect of co-doping of Na^{+} and Bi^{3+} ions on magnetotransport and thermopower studies of $La_{0.67}Sr_{0.33}MnO_3$ manganite," *Applied Physics A*, vol. 130, no. 11, Nov. 2024, Art. no. 811, https://doi.org/10.1007/s00339-024-07957-y.

[25] M. Khosrozadeh, Kh. Mabhouti, P. Norouzzadeh, and R. Naderali, "Complex impedance spectroscopy, dielectric response, and magnetic properties of the $La_{0.7}Sr_{0.3}BO_3$ (B = Mn, Fe, Co, or Ni) perovskite oxides," *Ceramics International*, vol. 50, no. 1, pp. 315–328, Jan. 2024, https://doi.org/10.1016/j.ceramint.2023.10.105.

[26] S. Suresh, P. S. Vindhya, and V. T. Kavitha, "A comprehensive study of dielectric, magnetic and anticancerous properties of lanthanum manganite perovskite nanoparticles," *Journal of Alloys and Compounds*, vol. 976, Mar. 2024, Art. no. 173222, https://doi.org/10.1016/j.jallcom.2023.173222.

[27] W. Xia, H. Wu, P. Xue, and X. Zhu, "Microstructural, Magnetic, and Optical Properties of Pr-Doped Perovskite Manganite $La_{0.67}Ca_{0.33}MnO_3$ Nanoparticles Synthesized via Sol-Gel Process," *Nanoscale Research Letters*, vol. 13, no. 1, Dec. 2018, Art. no. 135, https://doi.org/10.1186/s11671-018-2553-y.

[28] C. S. Ashok *et al.*, "The effect of B – site cation on the supercapacitive properties of $LaBO_3$ (B = Cr, Mn, Fe and Co) porous perovskites," *Journal of Energy Storage*, vol. 86, May 2024, Art. no. 111145, https://doi.org/10.1016/j.est.2024.111145.